Received: 25 August 2022 | Revised: 3 December 2022 | Accepted: 19 December 2022

DOI: 10.1002/nme.7192

RESEARCH ARTICLE

WILEY

Consistent splitting schemes for incompressible viscoelastic flow problems

Douglas R. Q. Pacheco[1] | **Ernesto Castillo**[2]

[1]Department of Mathematical Sciences, Norwegian University of Science and Technology, Trondheim, Norway

[2]Department of Mechanical Engineering, University of Santiago de Chile, Santiago, Chile

Correspondence
Douglas R. Q. Pacheco, Department of Mathematical Sciences, Norwegian University of Science and Technology, Trondheim, Norway.
Email: douglas.r.q.pacheco@ntnu.no

Funding information
Agencia Nacional de Investigacion y Desarrollo, Grant/Award Number: 1210156

[Correction added on 09 January 2023, after first online publication: The two hat symbols in Equation 14 have been corrected in this current version.]

Abstract

Viscoelastic fluids are highly challenging from the rheological standpoint, and their discretization demands robust, efficient numerical solvers. Simulating viscoelastic flows requires combining the Navier–Stokes system with a dynamic tensorial equation, increasing mathematical and computational demands. Hence, fractional-step methods decoupling the calculation of the flow quantities are an attractive option. In consistent fractional-step schemes, the splitting of the equations is derived from the continuous level, so that neither mass nor momentum balance is sacrificed. Thus, no corrections or velocity projections are needed, resulting in fewer algorithmic steps than other classical approaches. Moreover, consistency guarantees the absence of both numerical boundary layers and splitting errors, enabling high-order accuracy in space and time. This article introduces the first consistent splitting methods for incompressible flows of viscoelastic fluids, for which arbitrary constitutive laws are allowed. We present the formulation and the algorithm, along with various numerical examples testing their accuracy. First-, second- and third-order backward-differentiation schemes are numerically tested, and optimal convergence is confirmed for several spatial and temporal discretizations. Furthermore, good numerical stability is verified in challenging benchmark problems, including steady and time-dependent solutions.

KEYWORDS

consistent splitting, finite element method, fractional-step methods, high-order methods, viscoelastic fluids

1 | INTRODUCTION

The numerical approximation of viscoelastic fluids continues to be the greatest challenge in computational rheology today. Unlike generalized Newtonian fluids, viscoelastic fluids require the solution of a dynamic tensorial equation, coupled with the Navier–Stokes system. That results in an irreducible three-field problem requiring efficient and robust numerical techniques.[1,2] Despite recent attempts to reduce the problem through a viscosity-like tensor,[3] it is still unclear whether such models can appropriately represent viscoelastic behavior. Thus, an obvious motivation for decoupling the viscoelastic flow equations in time is reducing the overhead due to the additional tensor-valued field. Another key motivation

for decoupled strategies in high-elasticity regimes is the large differences between the velocity and stress time scales.[4,5] Therefore, it is of scientific interest to design methods that segregate the calculation of the unknowns.[6-8] Such decoupling schemes have lately become more common[9-12] and are currently the most effective way to enable large-scale viscoelastic flow simulations.

Unsteady flow simulations are several orders of magnitude more expensive than the corresponding steady-state cases. The computational fluid dynamics community has worked intensively to deliver more efficient time-dependent solvers in finite element, finite difference and finite volume methods. In this concern, the works of Chorin and Temam related to pressure-correction schemes were pioneers.[13,14] Decades later, Perot[15] applied ideas to the finite volume method as a unifier of time-decoupling schemes. Based on those studies, different schemes have been proposed, such as the velocity-correction schemes[16] and the Yosida-type ones[17] (see Reference 18 and the works cited therein for a comprehensive review).

Those methods were derived from semi-discrete and fully-discrete (or algebraic) approaches; some preserve the conservation of mass and affect the linear momentum equation, while others preserve the momentum balance. To retain all the properties of the continuous problem and allow higher-order temporal accuracy, Henshaw and Petersson[19] and Johnston and Liu[20] proposed a new family of methods. Guermond et al.[21] later coined the term "consistent splitting methods" to refer to those approaches, already suggesting that all other classical schemes had some inconsistency. Indeed, consistent splitting methods are based on a continuous reformulation of the Navier–Stokes system, allowing easy decoupling through extrapolation. Their full consistency frees these methods from splitting errors and numerical boundary layers, enabling higher-order accuracy in both space and time. Moreover, there is no need to correct the velocity or the pressure, resulting in fewer algorithmic steps than other methods such as incremental projection or Yosida. Although the analysis of consistent splitting methods is not as developed as in other classical approaches, there is significant numerical evidence of their stability, robustness and accuracy.[22] Extensions have been recently proposed for more complex flow scenarios, such as with generalized Newtonian fluids,[23,24] free-surface[25] or two-phase[26] flows, and fluid-structure interaction.[27] In this article, we present the first formulation for viscoelastic fluids.

Besides being computationally expensive, the fully coupled solution of viscoelastic flows is complex from the non-linear standpoint, which can be mitigated by splitting methods. Saramito[28] decoupled velocity and stresses with a scheme that involves a time approximation by alternating-direction implicit algorithms, using divergence-free Raviart–Thomas elements. The reported reduction of CPU time was remarkable, and more elastic regimes could be tackled compared to monolithic approaches. Chrispell et al.[29] then proposed a second-order θ-method for creeping viscoelastic flows, computing velocity, pressure and stresses in sequential substeps; the efficiency of solving smaller approximating systems in each substep was discussed in depth, including a priori error estimators. D'Avino et al.[7,30] proposed a decoupled, second-order temporal scheme for viscoelastic fluids considering inertial effects and zero solvent viscous contribution. In those references, the momentum and continuity equations are decoupled from the viscoelastic stress equation by replacing a time-discretized space-continuous form. Castillo and Codina,[31] on the other hand, employed an algebraic approach to design first-, second- and third-order pressure-correction-inspired methods using the Oldroyd-B and Giesekus models. In that article, the use of stabilized finite element formulations was discussed in detail for solving high Weissenberg number flows. Codina[10] later derived pressure-correction and velocity-correction methods at the purely algebraic level, using inexact *LU* factorization to estimate the formal decoupled-in-time error of each scheme. Nithiarasu[32] and He[33] extended the characteristic-based split scheme to viscoelastic fluid flows, including a stabilization to deal with the growth of elastic stresses.

In incompressible flow simulation, temporal integrators of order greater than two are somewhat unusual, and even completely absent in commercial engineering software. A reason for that is the conditional stability of higher-order schemes, which is called the second-order Dahlquist barrier.[34] Nonetheless, Ortega et al.[35] have demonstrated the benefits of using the third-order backward difference scheme (BDF3) for simulating mixed convection flows, while Vatsa et al.[36] showcased the capability of second- and third-order BDF schemes for turbulent flows. In that context, consistent splitting schemes offer a natural advantage since higher-order stepping can be implemented effortlessly.

In this work, we develop, implement and test a consistent splitting framework for incompressible viscoelastic fluid flows. The main ingredient is a consistent pressure Poisson equation (PPE) with consistent boundary conditions (BCs). This Poisson problem then replaces the divergence-free constraint, but incompressibility is kept unaffected at the continuous level. Due to its consistency and preserved incompressibility, this family of methods does not require any projections or correction steps. Hence, fewer algorithmic steps are needed in total. Furthermore, the inf-sup compatibility between pressure and velocity is not needed, so equal-order finite elements can be used without stabilization. Another advantage of this framework is that all the above-mentioned properties are independent of the viscoelastic constitutive law; in this

work, we use the Oldroyd-B model as proof of concept of the methodology. The proposed method uses BDF schemes of arbitrary temporal order to decouple all the unknown fields, which means that even the velocity and stress components are decoupled, resulting in schemes that require only the solution of scalar subproblems. Although we focus on finite elements for spatial discretization, any other methodology can be used.

We organize the rest of this article in the following manner. Section 2 presents the continuous viscoelastic Navier–Stokes problem and a PPE-based reformulation, proving the equivalence between them. In Section 3, we derive a weak formulation for the PPE and introduce the temporal integration schemes. In Section 4, the proposed fractional-step schemes are presented using the finite element method in space. Section 5 contains several numerical examples to test our framework; the tests are presented with increasing complexity, starting from problems with analytical solutions and moving on to more challenging benchmarks. Finally, we present concluding remarks in Section 6.

2 | STRONG FORMULATIONS

2.1 | Momentum-mass form

Let us consider a fluid-occupied domain Ω, which is an open set of $\mathbb{R}^d$ assumed to be bounded and polyhedral. Additionally, consider the time interval $(0, T]$, with $T < \infty$. The incompressible Navier–Stokes equations for an isothermal viscoelastic fluid can be written as

$$\nabla \cdot \boldsymbol{u} = 0 \qquad \text{in } \Omega \times (0, T] , \tag{1}$$

$$\partial_t \boldsymbol{u} + (\nabla \boldsymbol{u})\boldsymbol{u} - \beta \nu_0 \Delta \boldsymbol{u} - \nabla \cdot \boldsymbol{\sigma} + \nabla p = \boldsymbol{g} \qquad \text{in } \Omega \times (0, T] , \tag{2}$$

where $\boldsymbol{u}$ is the velocity vector field, p is the pressure, $\boldsymbol{g}$ is a given body force vector, and $\boldsymbol{\sigma}$ denotes the extra stress tensor. Consider also the dimensionless parameter $\beta \in [0, 1]$, used to define the effective (or solvent) viscosity $\beta\nu_0$ and the polymeric viscosity $(1 - \beta)\nu_0$, with ν_0 being the kinematic viscosity. For the momentum equation (2), we consider the following initial and boundary conditions

$$\boldsymbol{u} = \boldsymbol{u}_0 \qquad \text{at } t = 0 , \tag{3}$$

$$\boldsymbol{u} = \mathbf{u}_D \qquad \text{on } \Gamma_D \times (0, T] , \tag{4}$$

$$(\beta \nu_0 \nabla \boldsymbol{u})\boldsymbol{n} - p\boldsymbol{n} = \boldsymbol{\tau} \qquad \text{on } \Gamma_N \times (0, T] , \tag{5}$$

in which $\boldsymbol{n}$ is the outward unit normal vector, $\boldsymbol{u}_0$, $\boldsymbol{u}_D$ and $\boldsymbol{\tau}$ are known values defining the boundary and initial conditions, and Γ_D and Γ_N form a non-overlapping decomposition of the Lipschitz boundary $\Gamma := \partial\Omega$. We restrict ourselves to the Laplacian form of the momentum equation, as it allows easy decoupling of the velocity components. Note that bold characters are associated with vectors and tensors as notation.

The splitting methods presented herein are consistent regardless of the constitutive model used to define the symmetric stress tensor $\boldsymbol{\sigma}$. For concision, we will only deal with the classical Oldroyd-B model, in which each component σ_{ij} is given by

$$\partial_t \sigma_{ij} + \frac{\sigma_{ij}}{\lambda} + \boldsymbol{u} \cdot \nabla \sigma_{ij} = \frac{(1 - \beta)\nu_0}{\lambda} \left(\partial_{x_j} u_i + \partial_{x_i} u_j \right) + \sigma_{kj} \partial_{x_k} u_i + \sigma_{ik} \partial_{x_k} u_j , \tag{6}$$

where u_i refers to each of the d velocity components and $\lambda > 0$ is the relaxation time. The constitutive model selection is, in general, problem-dependent, and a possible reason to choose a particular model is the amount of elasticity of the fluid, which is related to the Weissenberg number. The numerical modeling of highly elastic fluids requires nonlinear viscoelastic models, such as Giesekus or Phan–Thien–Tanner, and additional mathematical treatments such as the log-conformation formulation. The key point in considering Equation (6) in our developments is its mathematical structure, which is the basis of nonlinear viscoelastic models and, therefore, the standard option for when new numerical methodologies are developed. Note that the fractional-step methods developed in this work are general, and any constitutive law can be adopted without significant effort. Although it is common practice to prescribe inlet boundary conditions for $\boldsymbol{\sigma}$, they are in principle not needed, so we do not consider any herein (see References 37 and 38 for a complete review

on the mathematical structure of the viscoelastic constitutive equations). On the other hand, an initial condition is needed for the stresses:

$$\boldsymbol{\sigma} = \boldsymbol{\sigma}_0 \quad \text{at} \quad t = 0 \,, \tag{7}$$

with $\boldsymbol{\sigma}_0 \in \mathbb{R}^{d\times d}_{\text{sym}}$ being a known value.

2.2 | Momentum-PPE reformulation

The first key ingredient for a consistent splitting scheme is defining a strong PPE to replace the explicit divergence-free constraint (1). We introduce the following Poisson problem:

$$-\Delta p = \nabla \cdot \left[\beta \nu_0 \nabla \times (\nabla \times \boldsymbol{u}) + (\nabla \boldsymbol{u})\boldsymbol{u} - \nabla \cdot \boldsymbol{\sigma} - \boldsymbol{g}\right] - \alpha \nabla \cdot \boldsymbol{u} \qquad \text{in } \Omega \times [0,T] \,, \tag{8}$$

$$\partial_n p = \boldsymbol{n} \cdot \left[\boldsymbol{g} - \partial_t \boldsymbol{u}_D - (\nabla \boldsymbol{u})\boldsymbol{u} - \beta \nu_0 \nabla \times (\nabla \times \boldsymbol{u}) + \nabla \cdot \boldsymbol{\sigma}\right] \qquad \text{on } \Gamma_D \times [0,T] \,, \tag{9}$$

$$p = \beta \nu_0 \nabla \boldsymbol{u} : (\boldsymbol{n} \otimes \boldsymbol{n} - \gamma \mathbf{I}) - \boldsymbol{\tau} \cdot \boldsymbol{n} \qquad \text{on } \Gamma_N \times [0,T] \,, \tag{10}$$

with $\alpha \geq 0$ and $\gamma \neq 0$ being user-defined parameters to be discussed later, and $\mathbf{I}$ denoting the $d \times d$ identity tensor. We will show that combining (2)–(5) with (8)–(10) leads to an equivalent system to the standard one (1)–(5), assuming all involved quantities are regular enough (see References 39 and 40 for details on regularity requirements). First, notice that this pressure Poisson system is consistent with the Navier–Stokes equations for any α and γ, in the sense that a sufficiently regular solution of (1)–(5) also fulfills (8)–(10). As a matter of fact, using Equation (1) and the following identities,

$$\begin{aligned}
[(\nabla \boldsymbol{u})\boldsymbol{n}] \cdot \boldsymbol{n} &= \nabla \boldsymbol{u} : (\boldsymbol{n} \otimes \boldsymbol{n}) \,, \\
\nabla \boldsymbol{u} : \mathbf{I} &= \nabla \cdot \boldsymbol{u} \,, \\
\Delta \boldsymbol{u} &= \nabla(\nabla \cdot \boldsymbol{u}) - \nabla \times (\nabla \times \boldsymbol{u}) \,, \\
\nabla \cdot (\partial_t \boldsymbol{u}) &= \partial_t (\nabla \cdot \boldsymbol{u}) \,,
\end{aligned}$$

the Poisson equation (8) and the Neumann BC (9) can be obtained from (2) and (4), while the Dirichlet BC (10) stems from the natural BC (5). Then, all we need for equivalence is to show that (2)–(5) and (8)–(10) imply $\nabla \cdot \boldsymbol{u} = 0$.

We begin by taking the divergence of both sides in Equation (2) and adding the result to Equation (8). Most terms cancel out, and we are left with

$$\partial_t (\nabla \cdot \boldsymbol{u}) = \beta \nu_0 \Delta (\nabla \cdot \boldsymbol{u}) - \alpha \nabla \cdot \boldsymbol{u} \,, \tag{11}$$

that is, a diffusion-reaction equation for the divergence of $\boldsymbol{u}$. We must then show that this equation admits only the trivial solution $\nabla \cdot \boldsymbol{u} = 0$. For $\beta = 0$ we get simply

$$\nabla \cdot \boldsymbol{u} = \mathrm{e}^{-\alpha t} \nabla \cdot \boldsymbol{u}_0 \,,$$

so that $\nabla \cdot \boldsymbol{u}$ will be zero for all t, provided that $\nabla \cdot \boldsymbol{u}_0 = 0$. A positive α can improve mass conservation at the discrete level by damping the growth of $\nabla \cdot \boldsymbol{u}$ due to approximation errors. For $\beta > 0$, Equation (11) requires boundary conditions for $\nabla \cdot \boldsymbol{u}$. Dotting Equation (2) by $\boldsymbol{n}$ and subtracting the result from (9) gives us the Neumann BC

$$\beta \nu_0 \partial_n (\nabla \cdot \boldsymbol{u}) = 0 \quad \text{on } \Gamma_D \,.$$

Similarly, we obtain a Dirichlet BC by dotting (5) by $\boldsymbol{n}$ and adding the result to (10):

$$\gamma \beta \nu_0 \nabla \cdot \boldsymbol{u} = 0 \quad \text{on } \Gamma_N \,.$$

Thus, Equation (11) will have zero boundary conditions if $\gamma \beta \nu_0 \neq 0$, so that with $\nabla \cdot \boldsymbol{u}_0 = 0$ we get $\nabla \cdot \boldsymbol{u} = 0$ for all t, as wanted.

We have now shown the equivalence of our PPE-momentum reformulation with respect to the standard Navier–Stokes formulation for any $\beta \geq 0$, $\alpha \geq 0$, and $\gamma \neq 0$. Notice that, for the pressure, the Dirichlet boundary Γ_D is a Neumann

boundary, whereas Γ_N becomes a Dirichlet boundary. It is possible to show that symmetry or free-slip boundaries Γ_S must be treated exactly as Γ_D, that is,

$$\partial_n p = \boldsymbol{n} \cdot \left[\boldsymbol{g} - (\nabla \boldsymbol{u})\boldsymbol{u} - \beta \nu_0 \nabla \times (\nabla \times \boldsymbol{u}) + \nabla \cdot \boldsymbol{\sigma}\right] \quad \text{on } \Gamma_S \times [0, T] \,,$$

where the boundary acceleration term has vanished because $\boldsymbol{u} \cdot \boldsymbol{n} = 0$ on Γ_S.

3 | WEAK FORM AND TIME DISCRETIZATION

As usual, the space of square-integrable functions in a domain Ω is denoted by $L^2(\Omega)$, while the space of functions with square-integrable gradient is $H^1(\Omega)$. Additionally, the brackets $\langle \cdot, \cdot \rangle_\omega$ are used to denote the product of two functions, integrated on ω (we omit the subscript when $\omega = \Omega$). If $f, g \in L^2(\Omega)$, we write the inner product as $\langle f, g \rangle = (f, g)$.

Since the PPE was obtained from the divergence of the momentum equation, it has higher-order derivatives which need to be eliminated if we want to use Lagrangian finite elements. To obtain an appropriate weak form, we start by multiplying Equation (8) with a test function q having zero trace on Γ_N. Integration by parts on both sides, together with the Neumann BC (9), yields

$$(\nabla p, \nabla q) = \langle \nabla q, \nabla \cdot \boldsymbol{\sigma} - (\nabla \boldsymbol{u})\boldsymbol{u} - \beta \nu_0 \nabla \times (\nabla \times \boldsymbol{u}) + \boldsymbol{g} \rangle - (q, \alpha \nabla \cdot \boldsymbol{u}) - \langle q, \boldsymbol{n} \cdot \partial_t \mathbf{u}_D \rangle_{\Gamma_D} \,.$$

Notice that some second-order derivatives remain, an issue overcome by Johnston and Liu[20] through the following identity:

$$-\langle \nabla q, \nabla \times (\nabla \times \boldsymbol{u}) \rangle = \langle \boldsymbol{n} \times \nabla q, \nabla \times \boldsymbol{u} \rangle_\Gamma \,,$$

for which a generalization exists when $\nabla \nu_0 \not\equiv \mathbf{0}$.[23,26] We finally obtain a weak formulation to compute p in terms of $\boldsymbol{u}$, $\boldsymbol{\sigma}$ and the problem data. The pressure problem consists in finding $p \in Z \subset H^1(\Omega)$ fulfilling (10), such that

$$(\nabla q, \nabla p) = (\nabla q, \nabla \cdot \boldsymbol{\sigma} - (\nabla \boldsymbol{u})\boldsymbol{u} + \boldsymbol{g}) - (q, \alpha \nabla \cdot \boldsymbol{u}) + \langle \boldsymbol{n} \times \nabla q, \beta \nu_0 \nabla \times \boldsymbol{u} \rangle_{\Gamma_N} - \langle q, \boldsymbol{n} \cdot \partial_t \mathbf{u}_D \rangle_{\Gamma_D} \tag{12}$$

holds for all $q \in Z$, with $q = 0$ on Γ_N. Although we will not discuss precise regularity requirements for the continuous problem, taking standard C^0 finite element spaces for all quantities will lead to a conforming discretization of (12). This matter was discussed by Johnston and Liu[20] for the Newtonian case, and no additional regularity is needed for viscoelastic fluids: having $q \in H^1(\Omega)$ in the PPE requires $\nabla \cdot \boldsymbol{\sigma} \in L^2(\Omega)$, which is fulfilled by taking $\boldsymbol{\sigma}$ in $H^1(\Omega)$ (or, in particular, in a continuous Lagrangian finite element space).

A consistent equation for the pressure allows great flexibility in designing stepping schemes: one can, in principle, construct implicit, semi-implicit or even fully explicit methods. We opt for semi-implicit schemes that are completely linearized and allow decoupling all unknowns as a series of scalar, iteration-free subproblems. Replacing the continuity equation with a consistent PPE does not lead to a CFL condition, even if the pressure term in the momentum equation is made explicit.[20] On the other hand, time-step restrictions may arise depending on how convective and stress terms are treated, as discussed in References 11,20, and 23. To decouple the velocity components and get a symmetric stiffness matrix for the velocity subproblems, we will treat convection explicitly, extrapolating $(\nabla \boldsymbol{u})\boldsymbol{u}$. Moreover, to separate $\boldsymbol{\sigma}$ and $\boldsymbol{u}$ and even decouple all stress components, we discretize the constitutive equation (6) in time as done by Ravindran,[11] see Section 4.2.

The decoupling is based on backward differentiation formulas and extrapolation rules of matching orders. Since consistent schemes have no splitting error, one can, in principle, consider temporal discretizations of arbitrary order. The BDF schemes with their respective extrapolation rules of order m can be written as

$$\partial_t \boldsymbol{u}|_{t=t_{n+1}} \approx \sum_{l=0}^{m} \delta_l \boldsymbol{u}^{n+1-l} \quad \text{and} \quad \boldsymbol{u}|_{t=t_{n+1}} =: \boldsymbol{u}^{n+1} \approx \hat{\boldsymbol{u}} = \sum_{l=1}^{m} \zeta_l \boldsymbol{u}^{n+1-l} \,,$$

where δ_l and ζ_l are finite-difference and extrapolation coefficients, respectively. The "hat" symbol indicates extrapolated quantities, and the coefficients for $m = 1, 2, 3$ (with constant time-step size Δt) are presented on Table 1. For a lighter presentation, we do not add any special notation for the discrete counterparts of $\boldsymbol{u}$, p and $\boldsymbol{\sigma}$, as we will henceforth only be dealing with the finite-dimensional problem.

TABLE 1 Extrapolation coefficients ζ_k and finite-difference coefficients δ_k (multiplied by the constant time-step size Δt) for backward differentiation schemes of order m.

m	$\delta_0\Delta t$	$\delta_1\Delta t$	$\delta_2\Delta t$	$\delta_3\Delta t$	ζ_1	ζ_2	ζ_3
1	1	−1	-	-	1	-	-
2	3/2	−2	1/2	-	2	−1	-
3	11/6	−3	3/2	−1/3	3	−3	1

4 | FRACTIONAL-STEP METHOD

The proposed fractional-step method consists of the three steps described below. A key point of this method is that only one algorithmic step per variable is needed, without the requirement for extra correction steps. The first step is associated with an equation for the velocity, the second with one for the stresses, and the third with one for the pressure.

4.1 | First step: Momentum equation

We will start every time step by computing the velocity components. For all test functions $\boldsymbol{v} \in [X_h]^d$ with $\boldsymbol{v}|_{\Gamma_D} = \boldsymbol{0}$, the weak form of the momentum equation reads

$$(\boldsymbol{v}, \partial_t \boldsymbol{u}) + (\nabla \boldsymbol{v}, \beta\nu_0 \nabla \boldsymbol{u}) = (\boldsymbol{v}, \nabla \cdot \boldsymbol{\sigma} - (\nabla \boldsymbol{u})\boldsymbol{u} + \boldsymbol{g}) - (\nabla \cdot \boldsymbol{v}, p\,) + \langle \boldsymbol{v}, \boldsymbol{\tau} \rangle_{\Gamma_N}, \tag{13}$$

with $X_h \subset H^1(\Omega)$ being a continuous finite element space. Notice that the extra stress term has not been integrated by parts, which is possible when using H^1-conforming finite elements for $\boldsymbol{\sigma}$. With that, we keep the natural boundary condition (5) unchanged, that is, without any contribution from $\boldsymbol{\sigma}$. Using an appropriate BDF scheme, we can further split the vectorial weak form (13) into d scalar equations. For each $i = 1, \ldots, d$ spatial component, we find $u_i^{n+1} \in X_h$ fulfilling (4), such that

$$\left(v, \delta_0 u_i^{n+1}\right) + \left(\nabla v, \beta\nu_0 \nabla u_i^{n+1}\right) = \left(v, \partial_{x_k} \widehat{\sigma_{ik}} + g_i^{n+1} - \widehat{\boldsymbol{u} \cdot \nabla u_i} - \sum_{l=1}^{m} \delta_l u_i^{n+1-l}\right) - \left(\partial_{x_i} v, \widehat{p}\,\right) + \left\langle v, \tau_i^{n+1} \right\rangle_{\Gamma_N} \tag{14}$$

for all $v \in X_h$, with $v = 0$ on Γ_N. By extrapolating the convective, stress and pressure terms, we are left with a linear problem to find each u_i^{n+1} component. Moreover, with explicit convection, we get d scalar linear subproblems with constant and symmetric stiffness matrices, which can be leveraged in computations. The d stiffness matrices are identical unless symmetry or slip conditions are considered, in which case the matrices can differ after the boundary conditions are enforced.

4.2 | Second step: Constitutive equation

With the velocity obtained at the first step, we can proceed to update the stresses. Using BDF formulas again, we can split the stress components by extrapolating all coupling terms, leading to

$$\left(\delta_0 + \frac{1}{\lambda} + \frac{1}{2}\nabla \cdot \boldsymbol{u}^{n+1}\right) \sigma_{ij}^{n+1} + \boldsymbol{u}^{n+1} \cdot \nabla \sigma_{ij}^{n+1} = f_{ij}^{n+1}, \tag{15}$$

with

$$f_{ij}^{n+1} := \frac{(1-\beta)\nu_0}{\lambda}\left(\partial_{x_j} u_i^{n+1} + \partial_{x_i} u_j^{n+1}\right) + \widehat{\sigma_{kj}}\, \partial_{x_k} u_i^{n+1} + \widehat{\sigma_{ik}}\, \partial_{x_k} u_j^{n+1} - \sum_{l=1}^{m} \delta_l \sigma_{ij}^{n+1-l}. \tag{16}$$

The velocity divergence on the left-hand side of Equation (15) is a consistent term added to ensure that the temporal stability of the stress equation be independent of incompressibility (see References 11 and 41 for details). Since Galerkin

formulations do not perform well without diffusion, we use a least-squares finite element method to tackle Equation (15). The problem consists in finding $\sigma_{ij} \in Y_h \subset H^1(\Omega)$ such that

$$\left(\kappa^{n+1} w + \boldsymbol{u}^{n+1} \cdot \nabla w \ , \ \kappa^{n+1} \sigma_{ij}^{n+1} + \boldsymbol{u}^{n+1} \cdot \nabla \sigma_{ij}^{n+1} - f_{ij}^{n+1}\right) = 0 \tag{17}$$

for all $w \in Y_h$, with $\kappa^{n+1} := \left(\delta_0 + \lambda^{-1} + \nabla \cdot \boldsymbol{u}^{n+1}/2\right)$. Mind that there is no need to extrapolate $\boldsymbol{u}$ here, since the current velocity $\boldsymbol{u}^{n+1}$ is already known at this point.

4.3 | Third step: Pressure update

Knowing both $\boldsymbol{u}^{n+1}$ and $\boldsymbol{\sigma}^{n+1}$ from the first and second steps, we can at last update the pressure. However, some care must be taken when $\Gamma_N \neq \emptyset$ and $\beta \neq 0$. In that case, for the pressure update we have a Dirichlet BC (10) depending on $\nabla \boldsymbol{u}^{n+1}$. The velocity gradient will be discontinuous when using Lagrangian finite elements, yet the pressure Dirichlet values must be continuous. There are several ways to circumvent that issue, for example through a continuous $L^2(\Gamma_N)$ projection of $\nabla \boldsymbol{u}^{n+1} : (\boldsymbol{n} \otimes \boldsymbol{n} - \gamma \mathbf{I})$.[23,42,43] Alternatively, we can compute a continuous $L^2(\Omega)$ projection of the (symmetric) velocity gradient, which is more expensive but simpler to implement than a boundary projection. This means replacing (10) by

$$p^{n+1} = \beta \nu_0 \mathbf{D}^{n+1} : (\boldsymbol{n} \otimes \boldsymbol{n} - \gamma \mathbf{I}) - \boldsymbol{\tau}^{n+1} \cdot \boldsymbol{n} \ \text{ on } \Gamma_N \ , \tag{18}$$

where $\mathbf{D}^{n+1}$ is a symmetric $d \times d$ tensor whose components $\mathrm{D}_{ij}^{n+1} \in Y_h$ are computed as

$$(\xi, 2\mathrm{D}_{ij}^{n+1}) = \left(\xi, \partial_{x_i} u_j^{n+1} + \partial_{x_j} u_i^{n+1}\right) \ \text{ for all } \ \xi \in Y_h \ . \tag{19}$$

Note that the projection (19) is the same used in the discrete elastic-viscous split-stress (DEVSS) method.[44]

The Dirichlet condition (18) also includes a factor γ not discussed yet. To show equivalence between the momentum-mass and momentum-PPE systems, we only assumed $\gamma \neq 0$. The most common approach[42] is to take $\gamma = 1$, but in our numerical tests, we have observed that a smaller value is often more stable when using higher-order temporal discretizations.

Finally, we compute $p^{n+1} \in Z_h$ fulfilling (18), such that

$$(\nabla q, \nabla p^{n+1}) = \left(\nabla q, \nabla \cdot \boldsymbol{\sigma}^{n+1} - (\nabla \boldsymbol{u}^{n+1}) \boldsymbol{u}^{n+1} + \boldsymbol{g}^{n+1}\right) - \left(q, \alpha \nabla \cdot \boldsymbol{u}^{n+1}\right) + \left\langle \boldsymbol{n} \times \nabla q, \beta \nu_0 \nabla \times \boldsymbol{u}^{n+1} \right\rangle_{\Gamma_N} - \left\langle q, \boldsymbol{n} \cdot \partial_t \mathbf{u}_D^{n+1} \right\rangle_{\Gamma_D} \tag{20}$$

for all $q \in Z_h$, with $q|_{\Gamma_N} = 0$. Notice that the pressure Poisson step is fully implicit because all necessary quantities at t_{n+1} are already known at the point of computing p^{n+1}. The factor $\alpha \geq 0$ in (20) can be interpreted as a penalizing term for large velocity divergences and can greatly improve mass conservation.[26] Different expressions have been proposed for this parameter,[25,26,45] and here we consider simply $\alpha = \mathcal{O}(\Delta t^{-1})$. An essential feature of consistent splitting methods is that no velocity projections are needed. Of course, the numerical solution $\boldsymbol{u}^{n+1}$ will not be exactly divergence-free, but any non-zero divergence values will be approximation errors.

4.4 | Fractional-step algorithm

We finally remark that the splitting scheme whose steps are presented in Sections 4.1–4.3 is just one of many possibilities enabled by having a consistent formulation. For instance, one may choose to compute the velocity and the extra stress in a coupled, implicit manner. Also, when the time scale for the stress evolution has a smaller order of magnitude than that of the velocity field, one might take several steps in the constitutive equation before moving on to the pressure and velocity substeps. Adaptive time-stepping is, of course, also possible.[23] The present method with its algorithmic steps is summarized in Algorithm 1.

Algorithm 1. Fractional-step method of order m

Compute the initial pressure using the PPE (12)
Set BDF order to $M = 1$
while $M < m$ **do**
  Step in time using a BDF scheme of order M
  Store current solution
  Increase BDF order to $M + 1$
end while
while $t < T$ **do**
  Increment time by Δt
  Extrapolate p, $\boldsymbol{\sigma}$, and $(\nabla \mathbf{u})\mathbf{u}$
  First step: calculate $\boldsymbol{u}$ using the momentum Equation (14)
  Second step: calculate $\boldsymbol{\sigma}$ using the constitutive Equation (17)
  Third step: calculate p using the PPE (12)
end while

4.5 | Adding stabilization terms

Although we do not aim to discuss stabilization methods (e.g., for dominant convection or elasticity), any consistent terms can, in principle, be incorporated into our framework. If the stabilization is not consistent, however, the equivalence between the mass-momentum and PPE-momentum systems may be compromised. To avoid that and retain consistency, the stabilization terms added to the momentum equation should also be incorporated into the PPE.

As an example, we present next the modification to the PPE when the DEVSS method is considered. To keep the momentum equation from becoming hyperbolic when $\beta << 1$, DEVSS adds to the left-hand side of (2) the term $(\beta - 1)\nu_0(\Delta \boldsymbol{u} - \nabla \cdot \mathbf{D})$, which is zero for vanishing mesh sizes. The stabilized momentum equation then reads[12]

$$(\boldsymbol{v}, \partial_t \boldsymbol{u}) + (\nabla \boldsymbol{v}, \nu_0 \nabla \boldsymbol{u}) = \langle \boldsymbol{v}, \nabla \cdot [\boldsymbol{\sigma} + (\beta - 1)\nu_0 \mathbf{D}] + \boldsymbol{g} - (\nabla \boldsymbol{u})\boldsymbol{u} \rangle - (\nabla \cdot \boldsymbol{v}, p\ ) + \langle \boldsymbol{v}, \boldsymbol{\tau} \rangle_{\Gamma_N}\,, \tag{21}$$

where $\mathbf{D}$ is computed exactly as in Equation (19). Since the added term is not formally consistent, we include it in the PPE system by modifying Equation (12) to

$$(\nabla q, \nabla p) \;=\; (\nabla q, \nabla \cdot [\boldsymbol{\sigma} + (\beta - 1)\nu_0 \mathbf{D}] - (\nabla \boldsymbol{u})\boldsymbol{u} + \boldsymbol{g}) - (q, \alpha \nabla \cdot \boldsymbol{u}) + \langle \boldsymbol{n} \times \nabla q, \nu_0 \nabla \times \boldsymbol{u} \rangle_{\Gamma_N} - \langle q, \boldsymbol{n} \cdot \partial_t \mathbf{u}_D \rangle_{\Gamma_D}\ . \tag{22}$$

We emphasize, however, that only (non-consistent) modifications to the momentum equation must be incorporated into the PPE. On the other hand, any model—stabilized or not—can be employed for the constitutive equation since no information on $\boldsymbol{\sigma}$ was used in our equivalence proof. This is important in the context of stabilized finite element formulations needed to approximate highly elastic viscoelastic fluids, where it has been numerically proven that including residual-based methods can introduce local instabilities when flows with a high elastic component are analyzed.[2,46-48]

5 | NUMERICAL EXAMPLES

This section uses numerical examples with increasing complexity to assess the accuracy of our schemes. Only two-dimensional examples are considered, with either first-order (linear or bilinear) or Taylor–Hood-type finite elements. We denote by $\mathbf{P}_a\mathrm{P}_b\mathbb{P}_c$ a simplicial finite element discretization with polynomial degrees a, b and c for $\boldsymbol{u}$, p and $\boldsymbol{\sigma}$, respectively, and analogously for quadrilateral elements $\mathbf{Q}_a\mathrm{Q}_b\mathbb{Q}_c$. All examples considered here have $b = c$ and $\boldsymbol{g} = \mathbf{0}$, that is, no body force. Unless otherwise stated, we set $\alpha = 1/\Delta t$ in the PPE (12). Moreover, whenever the term creeping flow is mentioned, it means that the convective term $(\nabla \boldsymbol{u})\boldsymbol{u}$ has been dropped.

5.1 | Convergence studies

The accuracy order of our schemes will be verified via problems with analytical solutions. Since viscoelastic flows with known solutions (and no manufactured body forces) are extremely scarce in the literature, we derive a new family based

on the Oldroyd-B model here. To allow solving the stress and velocity problems separately, we look for a solution such that $\sigma_{11} = \sigma_{22} = \sigma(t)$ and $\sigma_{12} = 0$. In that case, the momentum and constitutive equations reduce to

$$\partial_t \boldsymbol{u} + (\nabla \boldsymbol{u})\boldsymbol{u} - \beta \nu_0 \Delta \boldsymbol{u} + \nabla p = \boldsymbol{0} \,, \tag{23}$$

$$\sigma'(t) + \lambda^{-1}\sigma(t) = 2\left[\sigma(t) + (1-\beta)\nu_0\lambda^{-1}\right]\partial_{x_1} u_1 \,, \tag{24}$$

$$\sigma'(t) + \lambda^{-1}\sigma(t) = 2\left[\sigma(t) + (1-\beta)\nu_0\lambda^{-1}\right]\partial_{x_2} u_2 \,, \tag{25}$$

$$0 = 2\left[\sigma(t) + (1-\beta)\nu_0\lambda^{-1}\right](\partial_{x_1} u_2 + \partial_{x_2} u_1)/2 \,, \tag{26}$$

which will be satisfied by any incompressible flow $(\boldsymbol{u}, p)$ if we take

$$\lambda(t) = (\beta - 1)\frac{\nu_0}{\sigma(t)} > 0 \,, \tag{27}$$

that is, with a time-dependent relaxation time. Substituting (27) into (24) or (25) yields the Riccati equation

$$\sigma'(t) + \frac{\beta - 1}{\nu_0}\sigma^2(t) = 0 \,,$$

from which we get

$$\sigma(t) = -\frac{|\sigma_0|}{1 + t/\lambda_0} \quad \text{and} \quad \lambda(t) = t + \lambda_0 \,, \tag{28}$$

with $\sigma_0 < 0$ being the initial stress ($\sigma_{11}|_{t=0} = \sigma_{22}|_{t=0} = \sigma_0$) and $\lambda_0 = (1-\beta)\nu_0/|\sigma_0|$.

We then have a closed-form solution for the Oldroyd-B problem, requiring only a time-dependent λ, which is very simple to implement. Moreover, since no assumptions on $(\boldsymbol{u}, p)$ were made in the derivation and $\nabla \cdot \boldsymbol{\sigma}(t) \equiv \boldsymbol{0}$, any (incompressible) Newtonian velocity-pressure solution can be used. Notice, however, that since $\lambda(t)$ is an increasing function, setting a large final time T might lead to unreasonably high Weissenberg numbers—unless we have a decaying velocity field, as in Sections 5.1.2 and 5.1.3. This family of problems will be used to design numerical examples with different choices for the flow field $(\boldsymbol{u}, p)$. In the convergence studies, unless otherwise stated, we consider solutions of such type, with $\Gamma_N = \emptyset$ and $\alpha = 0$ in Equation (20).

5.1.1 | Temporal convergence

To verify our schemes' temporal accuracy, we use an exact solution that, at each time t, is fully resolved by the finite element spatial discretization—or, in other words, no spatial error exists. Although we omit the derivation, the reader can verify that

$$\boldsymbol{u} = \begin{pmatrix} a x_2 \\ a x_1 \end{pmatrix} f(t) \quad \text{and} \quad p = (b - a x_1 x_2) f'(t)$$

are a solution of the creeping flow problem for any given $a, b \in \mathbb{R}$ and any differentiable $f : \mathbb{R} \to \mathbb{R}$. For this example, we set $f(t) = \sin^2(5\pi t)$ and use the parameters given on Table 2, from which we compute the data $(\boldsymbol{u}_D, \boldsymbol{u}_0, \boldsymbol{\sigma}_0)$. Since for any given t we have constant $\boldsymbol{\sigma}$, linear $\boldsymbol{u}$ and bilinear p, any orthogonal $\mathbf{Q}_1\mathrm{Q}_1\mathbb{Q}_1$ mesh is sufficient to resolve the exact solution in space. We discretize Ω into four identical squares and consider BDF1, BDF2 and BDF3 schemes. The time interval is first divided into 30 equal segments ($\Delta t = 0.025$), and with each refinement level we divide Δt by 2. The error plots in Figure 1 confirm optimal temporal convergence of all unknowns for each of the BDF schemes.

TABLE 2 Problem data for the temporal convergence test.

ν_0	β	λ_0	T	a	b	Ω
1.0	0.2	0.1	0.75	1.0	0.25	$(0,1)^2$

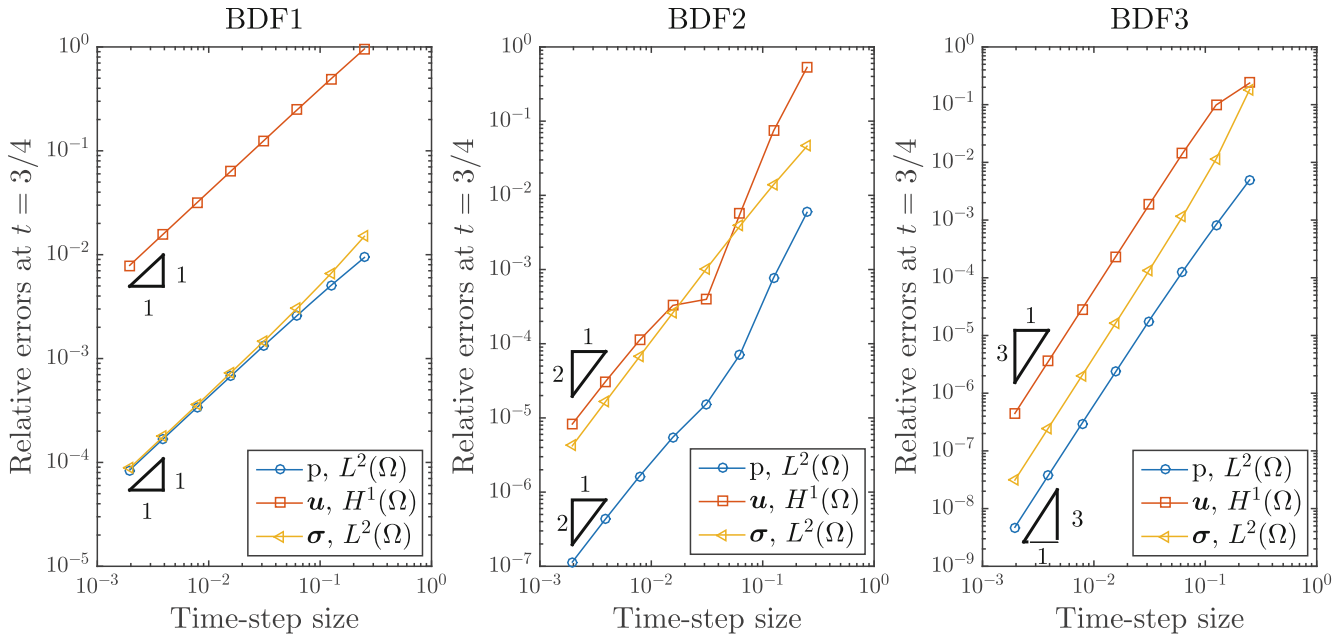

FIGURE 1 Temporal convergence study for the first-, second-, and third-order schemes, confirming optimal convergence.

TABLE 3 Problem data for the spatial convergence test.

ν_0	β	λ_0	T	Ω
0.1	0.5	0.5	1.0	$(0,1)^2$

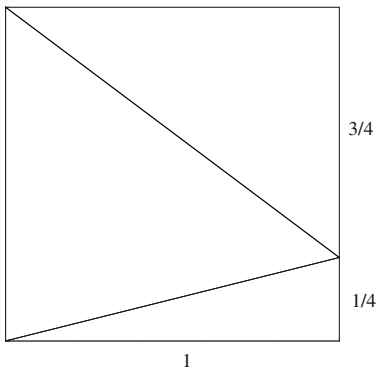

FIGURE 2 Taylor–Green flow with decaying stresses: Grid used as starting point for the refinement study.

5.1.2 | Spatial convergence

To assess spatial convergence, we consider a problem whose exact solution for $(\boldsymbol{u}, p)$ is non-polynomial. In $\Omega = (0,1)^2$, the Taylor–Green vortex is described by

$$\boldsymbol{u} = \begin{pmatrix} \sin \pi x_1 \cos \pi x_2 \\ -\sin \pi x_2 \cos \pi x_1 \end{pmatrix} \mathrm{e}^{-2\pi^2 \nu_0 \beta t} \quad \text{and} \quad p = \frac{\cos^2 \pi x_1 - \sin^2 \pi x_2}{2} \mathrm{e}^{-4\pi^2 \nu_0 \beta t},$$

for which we use the parameters from Table 3 and compute the corresponding Dirichlet and initial conditions. To avoid possible superconvergence phenomena,[49] we start the refinement study with a non-orthogonal grid (see Figure 2) and

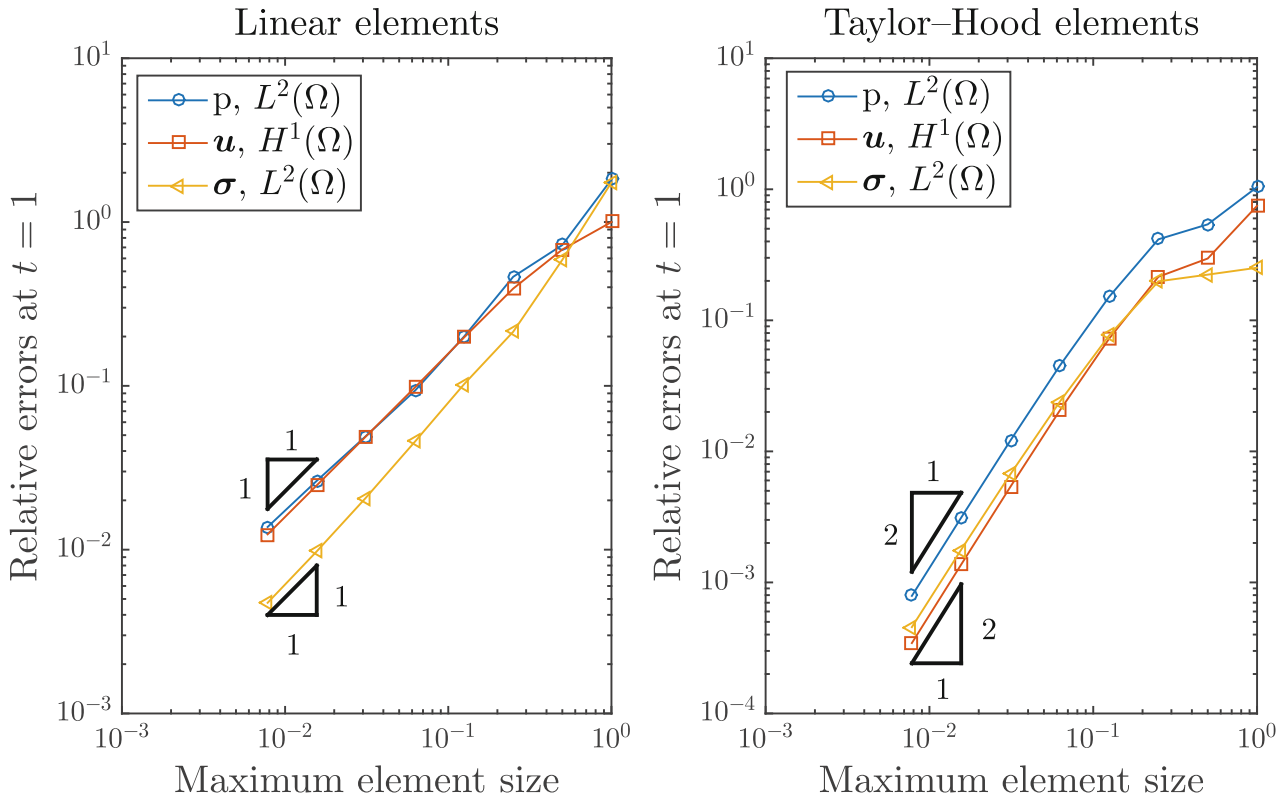

FIGURE 3 Taylor–Green flow with decaying stresses: Uniform mesh convergence study for linear ($\mathbf{P}_1\mathrm{P}_1\mathbb{P}_1$) and Taylor–Hood-type ($\mathbf{P}_2\mathrm{P}_1\mathbb{P}_1$) discretizations.

set $\alpha = 0$ in the PPE. The BDF3 temporal discretization starts with $\Delta t = 1/4$, and seven uniform refinements are then performed simultaneously in space and time. The results using both first-order and Taylor–Hood-type elements are shown in Figure 3, confirming the optimal convergence rates. At this point, it is important to note that the proposed methodology allows the use of arbitrary interpolations due to the complete decoupling of the velocity, pressure and stress fields. Additionally, using a third-order stepping scheme in these kinds of problems is rare, which is a distinctive feature of our work.

5.1.3 | The no-solvent case

As shown in Section 2.2, our PPE formulation is also consistent in the absence of viscous contribution from the solvent ($\beta = 0$). In that case, however, the second-order term would vanish from the momentum equation, making it hyperbolic—which we avoid via DEVSS (cf. Section 4.5). For the convergence test, we use the following radial flow:

$$\boldsymbol{u} = \begin{pmatrix} x_1/\lambda_0 \\ x_2/\lambda_0 \end{pmatrix} \frac{r^2 f(t)}{x_1^2 + x_2^2}, \quad \text{with} \quad f(t) = \frac{\lambda_0}{t + \lambda_0},$$

$$p = 2\left(\frac{r^2 f(t)}{R\lambda_0}\right)^2 \left[1 + \left(\frac{R}{2r}\right)^2 \log\left(\frac{x_1^2 + x_2^2}{R^2}\right) - \frac{(R/2)^2}{x_1^2 + x_2^2}\right],$$

in an annular domain with inner and outer radii r and R, respectively, and an opening angle of $\pi/8$, as illustrated in Figure 4. We omit the derivation again, but the reader can verify that this is a Navier–Stokes solution for any $\beta \geq 0$. Mind that even with an increasing relaxation time, the product $\lambda(t)\boldsymbol{u}$ does not vary with time, yielding a constant Weissenberg number. The remaining parameters are given on Table 4. We combine a family of linear triangular meshes with a BDF2 scheme, starting with $\Delta t = 0.014$ and refining uniformly in space and time for the convergence study. We obtain the expected linear convergence for all unknowns, as seen in Figure 4.

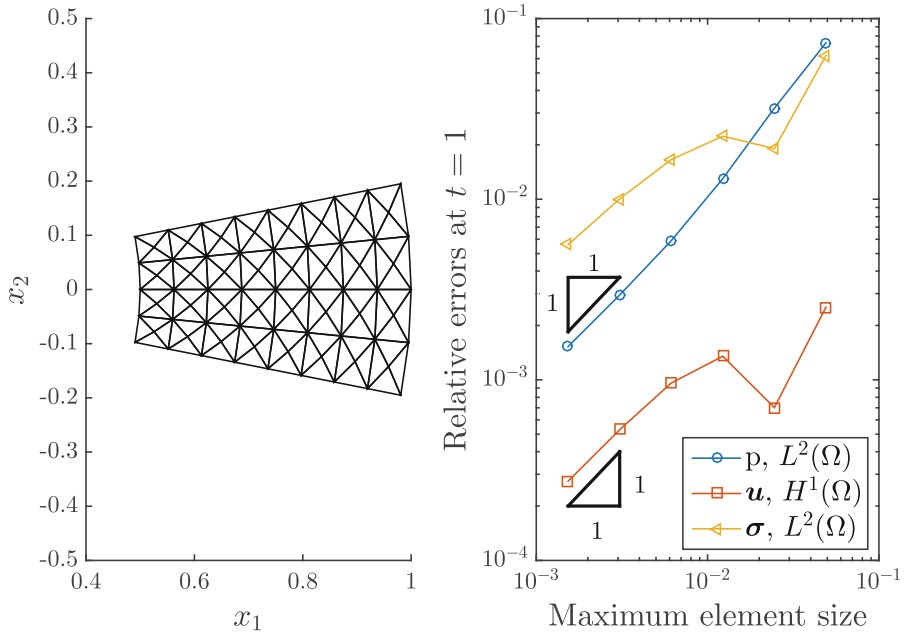

FIGURE 4 Radial flow with $\beta = 0$: Starting mesh (left) for the refinement study (right) using first-order elements with BDF2.

TABLE 4 Problem data for the no-solvent test case.

ν_0	β	λ_0	T	R	r
0.1	0.0	0.25	1.0	1.0	0.5

5.1.4 | Ramped up channel flow

For the last convergence test, we consider a symmetric channel flow in the domain $\Omega = (0, L) \times (0, H)$, with constant λ. The idea is to confirm the convergence rates in a more general setting combining wall, inlet, outlet and symmetry boundary conditions:

$$
\begin{aligned}
&\boldsymbol{u} = \boldsymbol{0} && \text{for } x_2 = H \text{ (no-slip)},\\
&u_2 = \partial_{x_2} u_1 = 0 && \text{for } x_2 = 0 \text{ (symmetry)},\\
&(\beta \nu_0 \nabla \boldsymbol{u})\boldsymbol{n} - p\boldsymbol{n} = \boldsymbol{0} && \text{for } x_1 = L \text{ (outflow)},\\
&\boldsymbol{u} = \begin{pmatrix} 1.5U[1 - (x_2/H)^2] f(t) \\ 0 \end{pmatrix} && \text{for } x_1 = 0 \text{ (inflow)},
\end{aligned}
$$

with

$$
f(t) = \frac{1 - \text{sign}(|2t - t^\star| - t^\star)}{2} \left[6\left(\frac{t}{t^\star}\right)^5 - 15\left(\frac{t}{t^\star}\right)^4 + 10\left(\frac{t}{t^\star}\right)^3 \right] + \frac{1 + \text{sign}(t - t^\star)}{2} \tag{29}
$$

increasing smoothly from zero (at $t = 0$) to one ($t \geq t^\star$). Since the time-dependent solution is not known, we set $t^\star = 2$ and compare the numerical results at $T = 10$ with the stationary solution

$$
\boldsymbol{u} = \begin{pmatrix} 1.5U[1 - (x_2/H)^2] \\ 0 \end{pmatrix}, \quad p = \frac{3U\nu_0}{H^2}(L - 2x_1),
$$

$$
\sigma_{11} = \frac{72(1-\beta)\lambda\nu_0 U^2}{H^4} x_2^2, \quad \sigma_{12} = -\frac{6(1-\beta)\lambda\nu_0 U}{H^2} x_2, \quad \sigma_{22} = 0,
$$

TABLE 5 Problem data for the channel flow test case.

ν_0	β	λ	T	$t^\star$	U	H	L
1.0	0.5	0.1	10.0	2.0	1.0	1.0	3.0

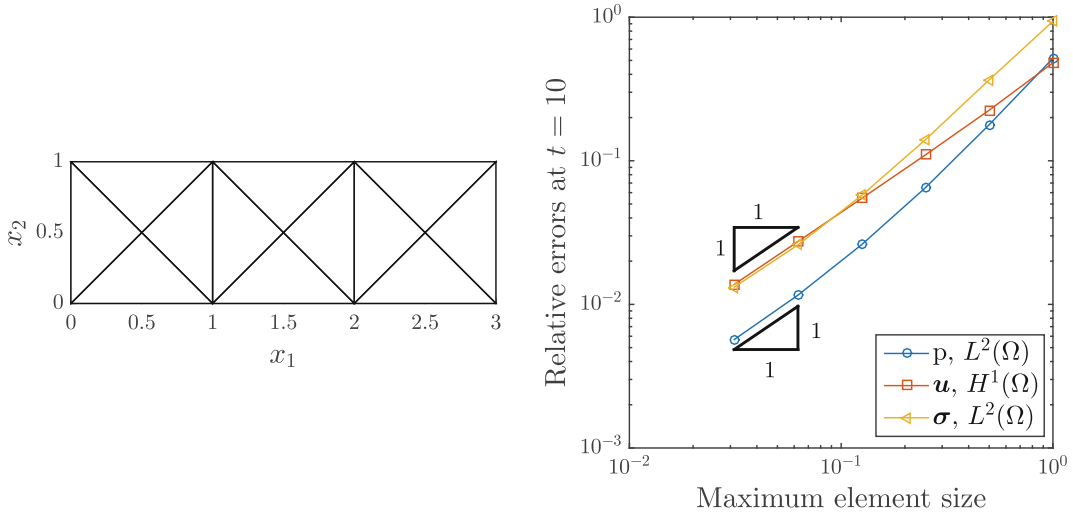

FIGURE 5 Ramped up channel flow: Starting mesh (left) for the uniform refinement study (right) using first-order elements and BDF1.

TABLE 6 Problem data for the cavity benchmark.

ν_0	β	λ	T	Ω
2.0	0.5	0.5	20.0	$(0,1)^2$

with the parameters given on Table 5. We set $\gamma = 0.1$ in the pressure BC (18). Using BDF1 and first-order triangular elements, the convergence study starts with $\Delta t = 1/24$ and twelve elements, as shown in Figure 5. Linear convergence is confirmed for all quantities.

5.2 | Lid-driven cavity flow

After having tested our schemes for flows with smooth exact solutions, we move on to more challenging problems. The first is the regularized lid-driven cavity flow, a classic viscoelastic benchmark.[50] On the unit square $\Omega = (0,1)^2$, we set $\boldsymbol{\sigma}_0 = \mathbf{0}$, $\boldsymbol{u}_0 = \mathbf{0}$ and

$$\boldsymbol{u}_D = \begin{pmatrix} 8[1+\tanh(8t-4)][(1-x_1)x_1]^2 \\ 0 \end{pmatrix} \quad \text{for} \quad x_2 = 1, \quad \boldsymbol{u}_D = \mathbf{0} \quad \text{elsewhere.}$$

The flow parameters are given on Table 6, which leads to a Weissenberg number of one half. This problem is known for its very sharp stress boundary layers, requiring extremely fine spatial resolution for converged results. We construct a graded mesh with 160×160 elements and the same nodes used by Pan et al.,[50] but with $\mathbf{Q}_2\mathrm{Q}_1\mathbb{Q}_1$ elements. The temporal discretization is first-order with $\Delta t = 0.005$. At $t = 20$, the flow is already at a steady state, and Figure 6 compares the lid stresses with those reported by Pan et al.,[50] showing excellent agreement. Mind that, even though we are not using any stabilization or log-conformation technique,[46,48] our results do not exhibit the spatial oscillations often seen for this problem.[51] In Figure 7, we show how σ_{11} varies along the cavity's depth, confirming the boundary layer's sharpness. The comparison in terms of the kinetic energy $E_k(t) := \langle \boldsymbol{u}, \boldsymbol{u} \rangle / 2$ is depicted in Figure 8, revealing good agreement throughout the whole simulation.

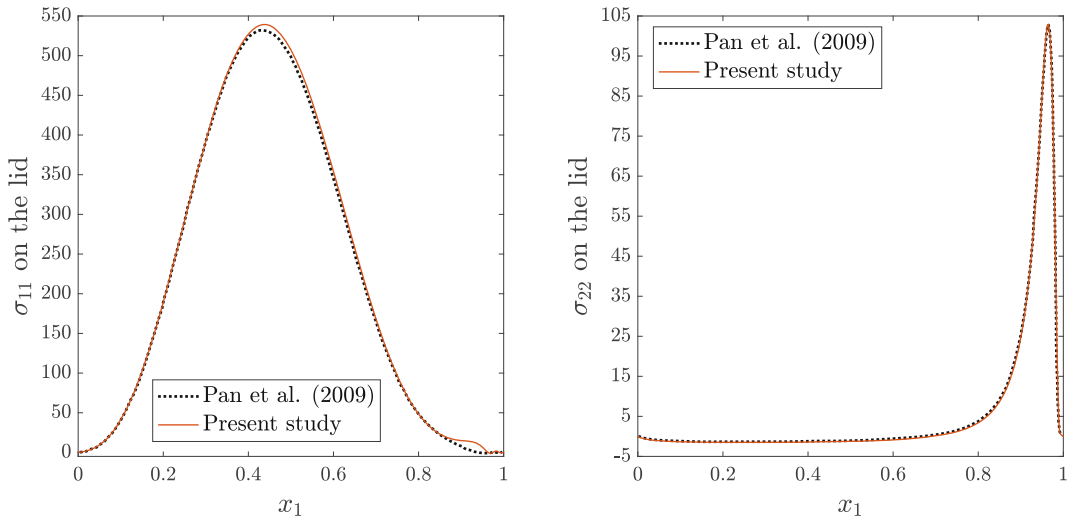

FIGURE 6 Lid-driven cavity flow at We = 0.5: Stress profiles on the lid, revealing very good agreement with reference results.[50]

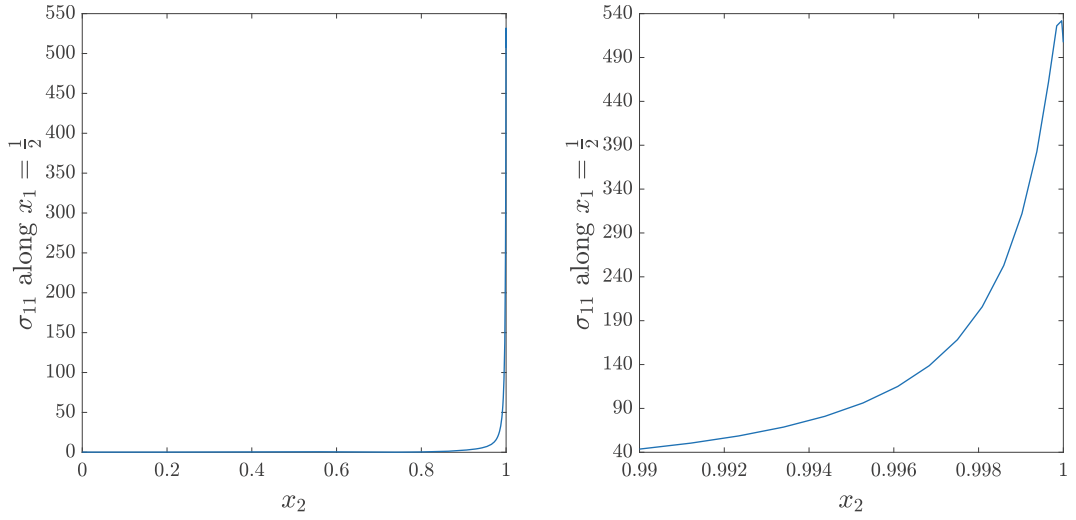

FIGURE 7 Lid-driven cavity flow at We = 0.5: Stress profile along the vertical center line, revealing a very sharp boundary layer (a dozen-fold decrease in σ_{11} within the first 1% of the cavity's depth).

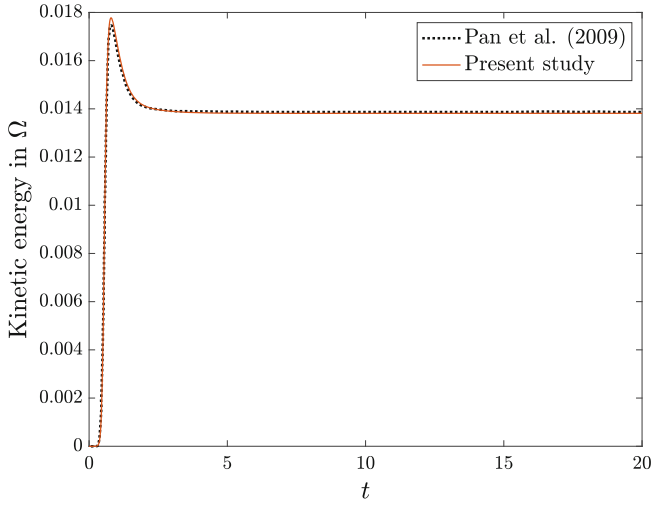

FIGURE 8 Lid-driven cavity flow at We = 0.5: Temporal evolution of the total kinetic energy, compared to reference results.[50]

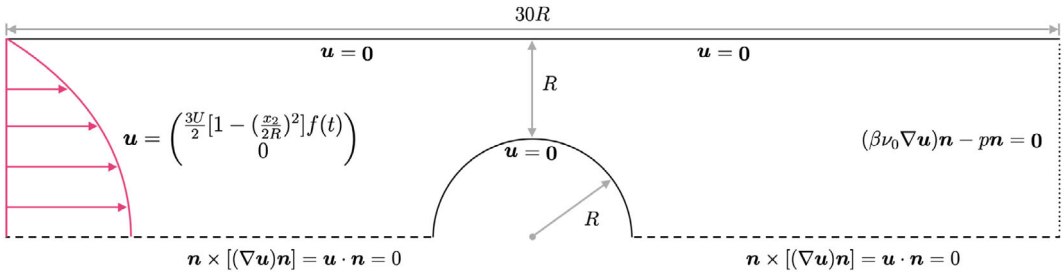

FIGURE 9 Creeping flow past a cylinder: Problem setup with the no-slip, symmetry, outlet and (ramped up (29)) inlet BCs.

TABLE 7 Problem data for the cylinder benchmark.

ν_0	β	$t^\star$	U	R	L
1.0	0.59	1.0	1.0	1.0	30.0

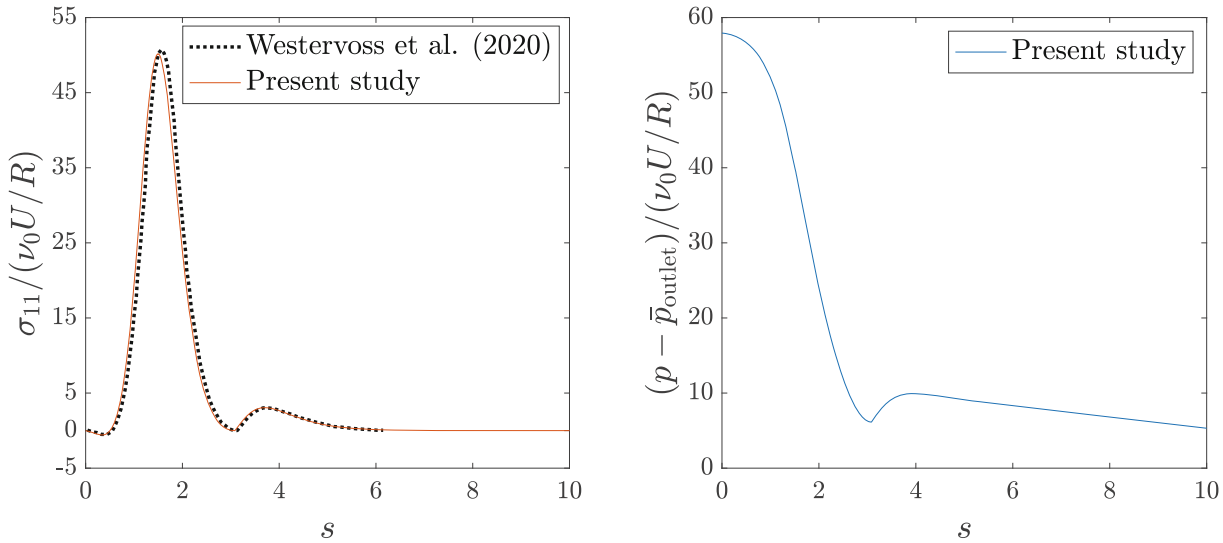

FIGURE 10 Creeping flow past a cylinder: Stress and pressure profiles for We = 0.3, along a parametrized arc-length curve starting at the cylinder's left-most point. The stress component σ_{11} is in very good agreement with the stationary results by Westervoß et al.,[3] both on the cylinder ($0 \leq s \leq \pi$) and along the wake ($s > \pi$). Mind that the pressure plotted on the right is relative to the mean outflow pressure.

5.3 | Creeping flow past a cylinder

One of the most popular and challenging benchmarks in viscoelasticity is the channel flow past a cylinder. The problem setup is described in Figure 9, with the inflow profile ramped up according to Equation (29). Denoting by R the cylinder's radius and by U the mean inflow velocity at $t = t^\star$, we set different values for the Weissenberg number $\mathrm{We} = \lambda U/R$. For the simulation, we consider $\gamma = 0.1$ and creeping flow with the parameters from Table 7. The time-step size is $\Delta t = 0.01$ and the mesh is structured, with 3.84×10^5 $\mathbf{P}_2\mathrm{P}_1\mathbb{P}_1$ elements of sizes between 0.004 and 0.02. For each Weissenberg number, the simulation is computed until a steady state is reached, which was possible up to We = 0.4; for higher values, spatial instabilities arose and eventually caused the simulation to break down. More elastic flows unavoidably need some stabilization technique, which is out of this work's scope.

In Figure 10, we plot σ_{11} and p along the arc-length curve s, which starts at the cylinder's left-most point and continues along Γ towards the outlet. The stress profile for We = 0.3 is in excellent agreement with the stationary results by Westervoß et al.[3] Notice that the pressure seen in the figure is relative to the mean outlet pressure $\overline{p}_{\mathrm{outlet}}$, which is zero in our case because $\boldsymbol{\tau} = \mathbf{0}$.[52]

TABLE 8 Creeping flow past a cylinder: Comparison between the present drag coefficients (at steady state, $t >> 1$) and the stationary results by Wittschieber et al.,[53] for different Weissenberg numbers.

We	Steady-state C_D	Stationary C_D[53]
0.1	130.336	130.329
0.2	126.600	126.617
0.3	123.167	123.202
0.4	120.567	120.617

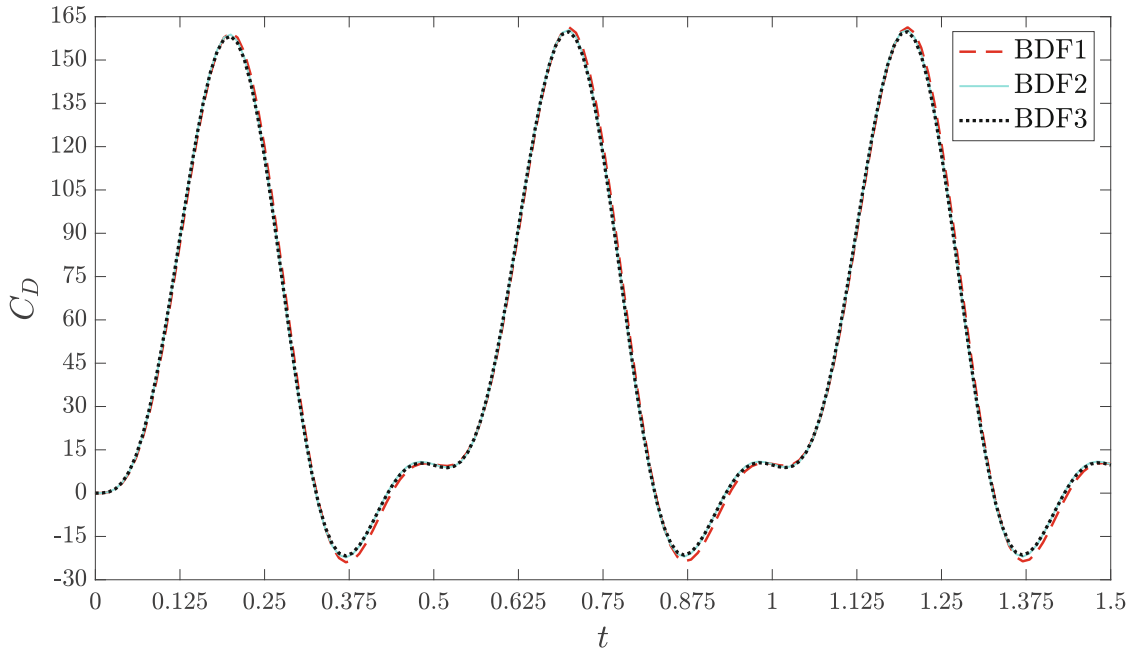

FIGURE 11 Periodic flow past a cylinder: Temporal evolution of the drag coefficient using different schemes in time.

For a more quantitative comparison, we compute the cylinder's drag coefficient C_D by

$$C_D = \frac{2}{\nu_0 U}\int_0^{\pi} \left(2\beta\nu_0\nabla^{\mathrm{s}}\boldsymbol{u} + \boldsymbol{\sigma} - p\mathbf{I}\right) : (-\boldsymbol{n}\otimes\boldsymbol{e}_1)\,\mathrm{d}s\,, \quad \text{with} \quad \boldsymbol{e}_1 = \begin{pmatrix}1\\0\end{pmatrix}.$$

Table 8 compares the results obtained in this work with those reported by Wittschieber et al.,[53] where SUPG stabilization was used. The drag coefficients show excellent agreement for the range of Weissenberg numbers considered here.

5.4 | Periodic flow past a cylinder

We now consider the periodic flow past a confined cylinder. The setup is equivalent to the previous example, but the inflow boundary condition is scaled by the periodic function $f(t) = \sin^4 2\pi t$ instead. We set We $= 0.1$, $\Delta t = 0.01$ and $\alpha = 0.1/\Delta t$, and do not turn off convection. The time-dependent drag coefficient in Figure 11 confirms the excellent agreement between the BDF1, BDF2 and BDF3 integrators, with the latter two giving practically overlapping solutions. We then use BDF3 with $\Delta t = 0.005$, and plot in Figure 12 the stress component σ_{12} at $t = 0.125$ (accelerating inflow), $t = 0.25$ (maximum inflow), $t = 0.375$ (decelerating inflow) and $t = 0.5$ (zero inflow). The stress isolines exhibit no oscillations, which showcases the spatial stability of our solution.

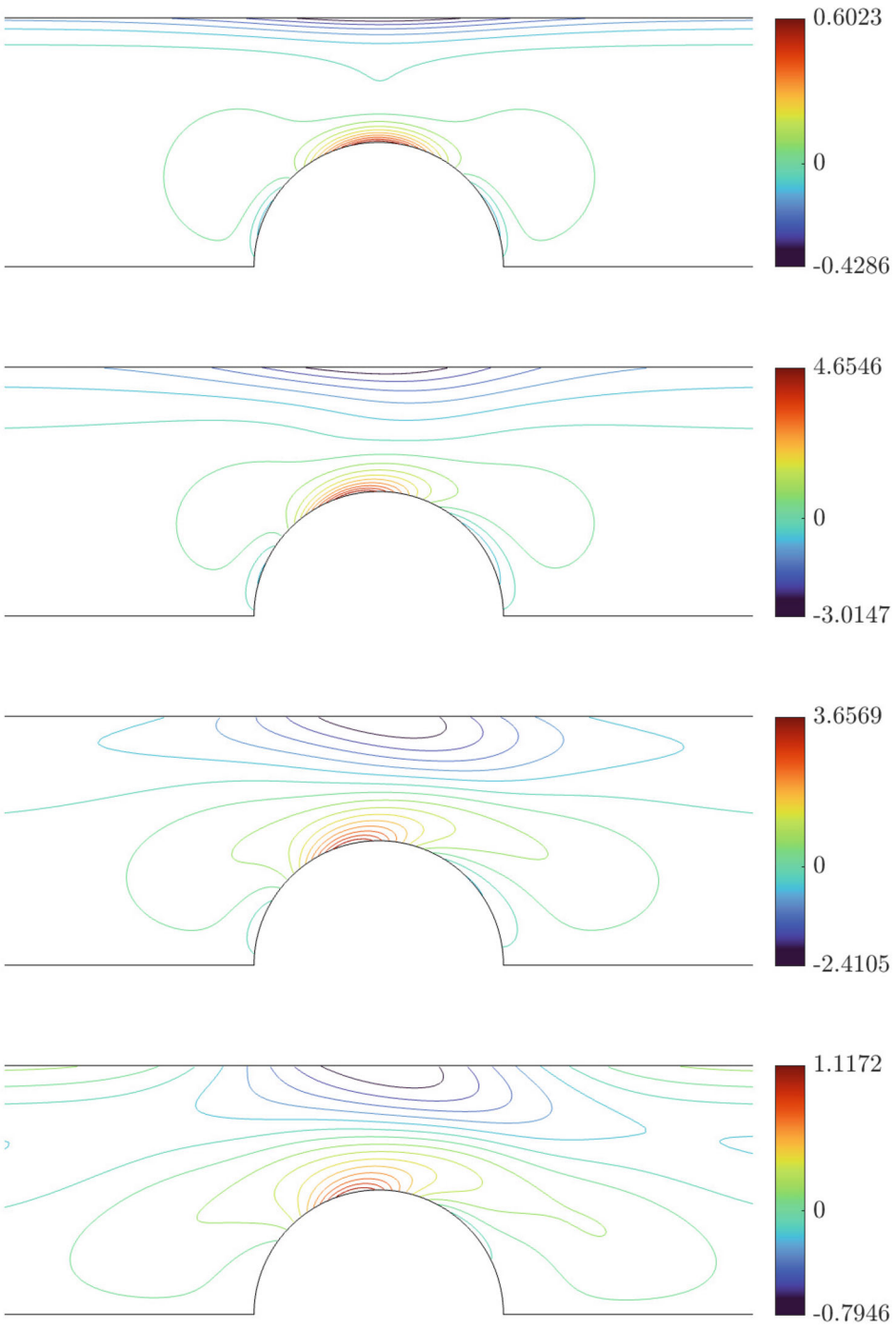

FIGURE 12 Periodic flow past a cylinder: σ_{12} isolines for $t = 0.125, 0.25, 0.375$, and 0.5, using BDF3.

6 | CONCLUDING REMARKS

In this work, we have developed, implemented and tested a consistent splitting framework for incompressible viscoelastic fluid flows. The proposed fractional-step methods allow the solution of each field—velocity, pressure and stress—in a fully decoupled manner and consists of only three steps, without requiring extra correction stages. Since the splitting of the equations is derived from the continuous level, mass and momentum balance are preserved. The consistency of the proposed methods eliminates splitting errors, allowing the use of time integration schemes with arbitrary order. Analytical manufactured solutions have been used to confirm optimal temporal convergence orders for all the unknown fields. The design of the method allows arbitrary finite element interpolations, which are tested with different time integration

schemes. First-, second- and third-order backward difference schemes are used in the numerical examples. The capability and robustness of the scheme are finally evaluated with the classical flow over a confined cylinder—steady-regularized and periodic—and the lid-driven benchmark problem.

The method presented here opens the path for higher-order—in both space and time—viscoelastic flow solvers. Another significant advantage is that we split the computation of each time step into scalar subproblems. This means that any open-source code that includes convection-diffusion problems can be adapted to solve viscoelastic fluids without significant changes in programming paradigm or data structure. Although our consistent pressure equation is slightly more complex than in classical projection methods, all the additional terms are on the right-hand side, that is, we still solve just a standard Poisson problem for the pressure. Future work includes combining our formulation with non-consistent stabilization methods to solve more complex viscoelastic constitutive models and efficiently achieve highly elastic flows.

ACKNOWLEDGMENT

The second author acknowledges the support given by the Agencia Nacional de Investigación y Desarrollo (ANID) through the project FONDECYT 1210156.

DATA AVAILABILITY STATEMENT

Data sharing is not applicable to this article as no new data were created or analyzed in this study.

REFERENCES

1. Barrenechea GR, Castillo E, Codina R. Time-dependent semidiscrete analysis of the viscoelastic fluid flow problem using a variational multiscale stabilized formulation. *IMA J Numer Anal*. 2019;39:792-819. doi:10.1016/j.compfluid.2016.07.012
2. Castillo E, Moreno L, Codina R, Baiges J. Stabilised variational multi-scale finite element formulations for viscoelastic fluids. *Arch Comput Methods Eng*. 2020;28:1987-2019. doi:10.1007/s11831-020-09526-x
3. Westervoß P, Turek S, Damanik H, Ouazzi A. The tensor diffusion approach for simulating viscoelastic fluids. *J Non-Newtonian Fluid Mech*. 2020;286:104431. doi:10.1016/j.jnnfm.2020.104431
4. Groisman A, Steinberg V. Elastic turbulence in a polymer solution flow. *Nature*. 2000;405:53-55. doi:10.1038/35011019
5. White CM, Mungal MG. Mechanics and prediction of turbulent drag reduction with polymer additives. *Annu Rev Fluid Mech*. 2008;40(1):235-256. doi:10.1146/annurev.fluid.40.111406.102156
6. Najib K, Sandri D. On a decoupled algorithm for solving a finite element problem for the approximation of viscoelastic fluid flow. *Numer Math*. 1995;72:223-238. doi:10.1007/s002110050167
7. D'Avino G, Hulsen MA, Maffettone PL. Decoupled transient schemes for viscoelastic fluid flow with inertia. *Comput Fluids*. 2012;66:183-193. doi:10.1016/j.compfluid.2012.06.023
8. Alves MA, Oliveira PJ, Pinho FT. Numerical methods for viscoelastic fluid flows. *Annu Rev Fluid Mech*. 2021;53(1):509-541. doi:10.1146/annurev-fluid-010719-060107
9. Al Mahbub MA, Hussain S, Nasu NJ, Zheng H. Decoupled scheme for non-stationary viscoelastic fluid flow. *Adv Appl Math Mech*. 2018;10:1191-1226. doi:10.4208/aamm.OA-2017-0186
10. Codina R. On the design of algebraic fractional step methods for viscoelastic incompressible flows. *Recent Advances in PDEs: Analysis, Numerics and Control*. SEMA SIMAI Springer Series. Springer; 2018:17 https://link.springer.com/chapter/10.1007/978-3-319-97613-6
11. Ravindran SS. Analysis of a second-order decoupled time-stepping scheme for transient viscoelastic flow. *Int J Numer Anal Model*. 2020;17(1):87-109.
12. Chai Y, Ouyang J, Wang X. An efficient stabilized finite element scheme for simulating viscoelastic flows. *Int J Numer Methods Fluids*. 2021;93(6):1947-1968. doi:10.1002/fld.4961
13. Chorin AJ. Numerical solution of the Navier-Stokes equations. *Math Comput*. 1968;22:745-762. doi:10.2307/2004575
14. Temam R. Sur l'approximation de la solution des équations de Navier-Stokes par la méthode des pas fractionnaires II. *Arch Ration Mech Anal*. 1969;33:377-385. doi:10.1007/BF00247696
15. Perot JB. An analysis of the fractional step method. *J Comput Phys*. 1993;108(1):51-58. doi:10.1006/jcph.1993.1162
16. Guermond JL, Shen J. Velocity-correction projection methods for incompressible flows. *SIAM J Numer Anal*. 2003;41(1):112-134. doi:10.1137/S0036142901395400
17. Quarteroni A, Saleri F, Veneziani A. Analysis of the Yosida method for the incompressible Navier–Stokes equations. *J Math Pures Appl*. 1999;78:473-503. doi:10.1016/S0021-7824(99)00027-6
18. Badia S, Codina R. Algebraic pressure segregation methods for the incompressible Navier-Stokes equations. *Arch Comput Methods Eng*. 2007;15:1-52. doi:10.1007/BF0302494
19. Henshaw WD, Petersson NA. *A Split-Step Scheme for the Incompressible Navier-Stokes Equations*. World Scientific; 2003:108-125.
20. Johnston H, Liu J-G. Accurate, stable and efficient Navier–Stokes solvers based on explicit treatment of the pressure term. *J Comput Phys*. 2004;199(1):221-259. doi:10.1016/j.jcp.2004.02.009
21. Guermond JL, Minev P, Jie S. An overview of projection methods for incompressible flows. *Comput Methods Appl Mech Eng*. 2006;195(44-47):6011-6045. doi:10.1016/j.cma.2005.10.010

22. Wu K, Huang F, Shen J. A new class of higher-order decoupled schemes for the incompressible Navier-Stokes equations and applications to rotating dynamics. *J Comput Phys*. 2022;458. doi:10.1016/j.jcp.2022.111097
23. Pacheco DRQ, Schussnig R, Fries T-P. An efficient split-step framework for non-Newtonian incompressible flow problems with consistent pressure boundary conditions. *Comput Methods Appl Mech Eng*. 2021;382:113888. doi:10.1016/j.cma.2021.113888
24. Bašić M, Blagojević B, Peng C, Bašić J. Lagrangian differencing dynamics for time-independent non-Newtonian materials. *Materials*. 2021;14(20):6210. doi:10.3390/ma14206210
25. Bašić J, Degiuli N, Blagojević B, Ban D. Lagrangian differencing dynamics for incompressible flows. *J Comput Phys*. 2022;111198. doi:10.1016/j.jcp.2022.111198
26. Pacheco DRQ, Schussnig R. Consistent pressure Poisson splitting methods for incompressible multi-phase flows: eliminating numerical boundary layers and inf-sup compatibility restrictions. *Comput Mech*. 2022. doi:10.1007/s00466-022-02190-x
27. Schussnig R, Pacheco DRQ, Fries T-P. Efficient split-step schemes for fluid–structure interaction involving incompressible generalised Newtonian flows. *Comput Struct*. 2022;260. doi:10.1016/j.compstruc.2021.106718
28. Saramito P. A new θ-scheme algorithm and incompressible FEM for viscoelastic fluid flows. *ESAIM Math Model Numer Anal*. 1994;28(1):1-35. doi:10.1051/m2an/1994280100011
29. Chrispell JC, Ervin VJ, Jenkins EW. A fractional step θ-method approximation of time-dependent viscoelastic fluid flow. *J Comput Appl Math*. 2009;232:159-175. doi:10.1016/j.cam.2009.05.024
30. D'Avino G, Hulsen MA. Decoupled second-order transient schemes for the flow of viscoelastic fluids without a viscous solvent contribution. *J Non-Newtonian Fluid Mech*. 2010;165(23):1602-1612. doi:10.1016/j.jnnfm.2010.08.007
31. Castillo E, Codina R. First, second and third order fractional step methods for the three-field viscoelastic flow problem. *J Comput Phys*. 2015;296:113-137. doi:10.1016/j.jcp.2015.04.027
32. Nithiarasu P. A fully explicit characteristic based split (CBS) scheme for viscoelastic flow calculations. *Int J Numer Methods Eng*. 2004;60(5):949-978. doi:10.1002/nme.993
33. He T. The cell-based smoothed finite element method for viscoelastic fluid flows using fractional-step schemes. *Comput Struct*. 2019;222:133-147. doi:10.1016/j.compstruc.2019.07.007
34. Dahlquist GG. A special stability problem for linear multistep methods. *BIT Numer Math*. 1963;3(1):27-43. doi:10.1007/BF01963532
35. Ortega E, Castillo E, Cabrales RC, Moraga NO. Effect of time integration scheme in the numerical approximation of thermally coupled problems: from first to third order. *Comput Math Appl*. 2021;99:345-360. doi:10.1016/j.camwa.2021.08.018
36. Vatsa V, Carpenter M, Lockard D. Re-evaluation of an optimized second order backward difference (BDF2OPT) scheme for unsteady flow applications. Proceedings of the 48th AIAA Aerospace Sciences Meeting Including the New Horizons Forum and Aerospace Exposition; 2010. doi: 10.2514/6.2010-122
37. Renardy M. Mathematical Analysis of Viscoelastic Flows. Regional Conference Series in Applied Mathematics; 1989.
38. Fernández-Cara E, Guillén F, Ortega RR. Mathematical modeling and analysis of viscoelastic fluids of the Oldroyd kind. *Handbook of Numerical Analysis*. Vol VIII. North-Holland; 2002.
39. Heywood JG, Rannacher R. Finite element approximation of the nonstationary Navier–Stokes problem. I. Regularity of solutions and second-order error estimates for spatial discretization. *SIAM J Numer Anal*. 1982;19:353-384. https://www.jstor.org/stable/2157967
40. Sani RL, Shen J, Pironneau O, Gresho PM. Pressure boundary condition for the time-dependent incompressible Navier–Stokes equations. *Int J Numer Methods Fluid*. 2006;50(6):673-682. doi:10.1002/fld.1062
41. Guermond J-L, Quartapelle L. A projection FEM for variable density incompressible flows. *J Comput Phys*. 2000;165(1):167-188. doi:10.1006/jcph.2000.6609
42. Liu J. Open and traction boundary conditions for the incompressible Navier–Stokes equations. *J Comput Phys*. 2009;228(19):7250-7267. doi:10.1016/j.jcp.2009.06.021
43. Plasman L, Deteix J, Yakoubi D. A projection scheme for Navier-Stokes with variable viscosity and natural boundary condition. *Int J Numer Methods Fluid*. 2020;92(12):1845-1865. doi:10.1002/fld.4851
44. Guénette R, Fortin M. A new mixed finite element method for computing viscoelastic flows. *J Non-Newtonian Fluid Mech*. 1995;60:27-52. doi:10.1016/0377-0257(95)01372-3
45. Li L. A split-step finite-element method for incompressible Navier-Stokes equations with high-order accuracy up-to the boundary. *J Comput Phys*. 2020;408:109274. doi:10.1016/j.jcp.2020.109274
46. Castillo E, Codina R. Variational multi-scale stabilized formulations for the stationary three-field incompressible viscoelastic flow problem. *Comput Methods Appl Mech Eng*. 2014;279:579-605. doi:10.1016/j.cma.2014.07.006
47. Castillo E, Codina R. Finite element approximation of the viscoelastic flow problem: a non-residual based stabilized formulation. *Comput Fluids*. 2017;142:72-78. doi:10.1016/j.compfluid.2016.07.012
48. Moreno L, Codina R, Baiges J, Castillo E. Logarithmic conformation reformulation in viscoelastic flow problems approximated by a VMS-type stabilized finite element formulation. *Comput Methods Appl Mech Eng*. 2019;354:706-731. doi:10.1016/j.cma.2019.06.001
49. Pacheco DRQ, Steinbach O. On the initial higher-order pressure convergence in equal-order finite element discretizations of the Stokes system. *Comput Math Appl*. 2022;109:140-145. doi:10.1016/j.camwa.2022.01.022
50. Pan T-W, Hao J, Glowinski R. On the simulation of a time-dependent cavity flow of an Oldroyd-B fluid. *Int J Numer Methods Fluids*. 2009;60(7):791-808. doi:10.1002/fld.1919
51. Venkatesan J, Ganesan S. A three-field local projection stabilized formulation for computations of Oldroyd-B viscoelastic fluid flows. *J Non-Newtonian Fluid Mech*. 2017;247:90-106. doi:10.1016/j.jnnfm.2017.06.007

52. Heywood JG, Rannacher R, Turek S. Artificial boundaries and flux and pressure conditions for the incompressible Navier-Stokes equations. *Int J Numer Methods Fluids*. 1996;22(5):325-352.
53. Wittschieber S, Demkowicz L, Behr M. Stabilized finite element methods for a fully-implicit logarithmic reformulation of the Oldroyd-B constitutive law. *J Non-Newtonian Fluid Mech*. 2022;306:104838. doi:10.1016/j.jnnfm.2022.104838

How to cite this article: Pacheco DRQ, Castillo E. Consistent splitting schemes for incompressible viscoelastic flow problems. *Int J Numer Methods Eng*. 2023;124(8):1908-1927. doi: 10.1002/nme.7192